J Mater Sci: Mater Electron (2016) 27:7707–7714
DOI 10.1007/s10854-016-4757-1

Electrochemical preparation and supercapacitive performance of α-MnO_2 nanospheres with secondary wall-like structures

Mustafa Aghazadeh[1] · Mohammad Ghannadi Maragheh[1] · Mohammad Reza Ganjali[2,3] · Parviz Norouzi[2] · Davoud Gharailou[2] · Farnoush Faridbod[2]

Received: 11 January 2016 / Accepted: 30 March 2016 / Published online: 5 April 2016

Abstract A new approach has been proposed for the preparation of nanostructured α-MnO_2. The method is based on the galvanostatic cathodic electrodeposition of the product from a nitrate bath under a direct current mode at a current density of 0.1 mA cm^{-2}. The intermediate product deposited in this stage is next thermally treated at 300 °C for 3 h. To evaluate the properties of the final product, it was characterized by XRD and FTIR so as to gain information on its phase composition (which was found to be mainly α-MnO_2) and SEM to gain information on its morphology (which was found to be nanospheres with secondary porous wall-like nanostructures). Additional electrochemical experiments on the product through cyclic voltammetry and charge–discharge tests revealed it to be capable of delivering high specific capacitance of 280 F g^{-1}, further its outstandingly long-term cycling stability which was only diminished to 95.4 % of the initial value after 1000 discharge cycles.

1 Introduction

The application of MnO_2 as the electrode materials in the construction of electrochemical supercapacitors is subject to a great deal of interest, due it's the high specific capacitance value, low cost and environmental compatibility [1–4]. MnO_2 is available in five various crystal structures named α, β, γ, λ and δ which can directly influence the supercapacitive behavior of the MnO_2 electrodes in electrochemical supercapacitors [5–8].

The two charge storage mechanisms proposed for MnO_2 electrode materials in aqueous electrochemical supercapacitor are mentioned below [9]; The former mechanism suggests the surface adsorption of the cations present in the electrolyte (C^+) on the MnO_2 material, i.e.:

$$(\mathbf{MnO_2})_{\mathbf{surface}} + \mathbf{C^+} + \mathbf{e^-} \leftrightarrow \left(\mathbf{MnO_2^- C^+}\right)_{\mathbf{surface}} \quad (1)$$
$$C^+ = H^+,\ Na^+,\ K^+,\ Li^+$$

The later proposes the intercalation of H^+ or alkali metal cations (C^+) within the MnO_2 electrode material during the reduction step and a subsequent deintercalation which takes place during the oxidation step, i.e.:

$$\mathbf{MnO_2} + \mathbf{H^+} + \mathbf{e^-} \leftrightarrow \mathbf{MnOOH} \quad (2)$$

$$\mathbf{MnO_2} + \mathbf{C^+} + \mathbf{e^-} \leftrightarrow \mathbf{MnOOC} \quad (3)$$

As it is clear the first mechanism only considers the involvement of the surface Mn sites in the charge storage process, while the latter assigns this role to the bulk Mn sites. Both mechanisms, however, indicate that the MnO_2 material used in the electrodes need to have large surface areas and electronic conductivity values to be suitable for used in supercapacitors to utilize the theoretical specific capacitance (1370 F g^{-1}). It has been well established that α, β and γ phases of MnO_2 includes one dimensional path ways in their structures; the δ phase is a two dimensional layered compound, and the λ has a three dimensional spinel structure [10–13]. Based on the described mechanisms which are based on the intercalation/deintercalation of H^+ or alkali metal cations in the MnO_2, only the phases with

✉ Mustafa Aghazadeh
mustafa.aghazadeh@gmail.com; maghazadeh@aeoi.org.ir

[1] Nuclear Science and Technology Research Institute (NSTRI), P.O. Box 14395-834, Tehran, Iran

[2] Faculty of Chemistry, Center of Excellence in Electrochemistry, University of Tehran, Tehran, Iran

[3] Biosensor Research Center, Endocrinology and Metabolism Molecular-Cellular Sciences Institute, Tehran University of Medical Sciences, Tehran, Iran

sufficient gaps are of value for capacitance studies. In the case of such phases, the amount of H^+ or alkali metal cations which are intercalated/extracted determines the specific capacitance of the material, and hence the specific capacitance values are expected to be dependent on the size of pathways in the structure or the interlayer space of MnO_6 octahedral.

The difference in the structure of the different MnO_2 phases originates from the location of the MnO_6 octahedrons, which can lead to the formation of different empty spaces or gaps. The largest empty spaces are observed in the case of δ-MnO_2, in which case the interlayer separation reportedly reaches about 7 Å. The next phase is the α-MnO_2, which includes combinations of 1 × 1 and 2 × 2 tunnels, giving rise to interlayer separations ranging from about 1.89 to 4.6 Å. As it is evident from these discussions the minimal empty spaces are present in the γ and β phases, which contain a combination of 1 × 1 and 1 × 2 tunnels leading to interlayer separations ranging from 1.89 to 2.3 Å, respectively (in the case of the γ phase); 1 × 1 pathways with an average interlayer separation of 1.89 Å (in the case of the β phase) [11, 12]. SCVs of these phases have been experimentally determined to fall in the order of $\alpha \approx \delta > \gamma > \lambda > \beta$ [10]. Further evaluations on the crystal and electrochemical characteristics of the different MnO_2 phases by Musil et al. [14] have proven the capabilities of these structures to decline in the order of $\alpha > \gamma > \delta \approx \beta$. Putting all the facts stated above on can conclude that the largest pathways (i.e. 2 × 2 tunnels) in the case of the phase leaded to maximal facilitation of the intercalation/extraction phenomena, providing the material with unique properties for use in supercapacitor devices, which is very well reflected by the relatively large amount of efforts directed on this material in comparison to the other manganese dioxide phases [15–24] as well as the considerable research activities on developing simple and affective approaches to the preparation of α-MnO_2 especially in nanoscale, which further boost its supercapacitive performance.

Electrochemical methods can be the approaches taken for the synthesis of nanostructured α-MnO_2 with controlled morphologies and enhanced surface areas. Until now, different electrochemical routs have been applied in the synthesis of metal oxides (metal = Mn, Ni, Co, Fe, Zn, Ce,…) [25, 26]. Nanostructured MnO_2 can be prepared by cathodic or anodic deposition techniques [25]. There are intensive reports on the anodic deposition of MnO_2 and investigation of the electrochemical performance of the prepared nanostructures by this route [27–31]. However, in spite of the impressive progress achieved in the field of anodic electrosynthesis of MnO_2, anodic oxidation and dissolution of the substrates have been reported as the major problems of this method [32, 33]. These problems can be resolved by the development of cathodic electrodeposition methods, including (1) cathodic reduction of Mn^{7+} species in permanganate bath [34] and (2) base (OH^-) electrogeneration on the cathode [19, 35]. Cathodic electrodeposition via production of OH^- ions has a two-step electrochemical-chemical (EC) process [25, 36]. In the electrochemical step, OH^- ions are produced on the cathode surface resulting increases of pH value, and the deposit formation is occurred in the chemical step. The obtain deposit is then heat-treated to obtain final oxide product. The current work focuses on the application of a cathodic electrodeposition route for the production of pure α-MnO_2 of controlled morphology and supercapacitive characteristics through a galvanostatic deposition route ($I = 0.1$ mA cm^{-2}) followed by thermal-treatment at 300 °C. The prepared α-MnO_2 was further characterized by cyclic voltammetry (CV) and galvanostatic charge–discharge measurements, to evaluate the properties of the obtained α-MnO_2 in supercapacitive applications.

2 Experimental

2.1 Synthesis of MnO_2

Nanostructured MnO_2 was synthesized by a cathodic electrodeposition procedure in an electrochemical cell including a steel substrate cathode (316 L) located between two parallel counter–electrodes made of graphite. The cathode galvanostatically electropolished at a current density of 0.2 A cm^{-2} for 5 min in a bath (70 °C) containing 50 vol% phosphoric acid, 25 vol% sulfuric acid, and balanced deionized water, prior to the deposition. The depositions were performed in a galvanostatic mode at a current density of 0.1 mA cm^{-2} ($I = 0.1$ mA cm^{-2}) for 2 h. An aqueous solution of 0.005 M $Mn(NO_3)_2{\cdot}6H_2O$ (Merck) was used as the electrolyte. After deposition, the cathode was several times washed with distilled water, and dried at 50 °C for 4 h. The deposited product was then scraped from its surface and thermally treated. The thermal treatment was performed at 300 °C for 3 h under a dry air atmosphere in a programmable high temperature furnace.

2.2 Characterization experiments

The powder X-ray diffraction (XRD) analyses were performed by a Phillips PW-1800 diffractometer equipped with a Cu Kα radiation source (λ = 1.5406 Å) at a scanning rate of 5 degree/min. The FTIR spectra were acquired in the range of 400–4000 cm^{-1} using a Bruker Vector 22 spectroscope, while the samples were in a KBr wafer. Each spectrum was acquired after 20 scans at a resolution of 4 cm^{-1} under ambient temperature. Morphological studies

of the product were performed using a scanning electron microscope (SEM, LEO 1455 VP, Oxford, UK, operating voltage 30 kV). The SEM analyses included mounting a small amount of the produced oxide powder on a conducting carbon tape and sputter coating it with Au to improve the conductivity. The BET specific surface area data were collected based on the adsorption in a relative pressure range of 0.05–0.98, by a Quanta-chrome NOVA-2200e system. The average distributions of the pore sizes were calculated by the BJH method and all adsorption and desorption isotherms were obtained at −196 °C was after degassing the samples under vacuum at 110 °C for 5 h.

2.3 Electrochemical measurements

For the electrochemical measurements MnO_2-based working electrodes were used. These electrodes were constructed by first preparing a mixture of 85 wt% of the product with 10 wt% of carbon black and 5 wt% polytetrafluorene ethylene. Next a small volume of ethanol was added to this mixture to help homogenize it and the mixture was pressed onto a steel grid (0.5 cm × 0.5 cm) current collector. These were used as the working electrodes in electrochemical characterization experiments in a conventional three electrode cell containing a 1 M Na_2SO_4 solution as the electrolyte, as well as platinum foil and Ag/AgCl (saturated with 1 M KCl) electrodes as the counter and reference electrodes. The electrochemical measurements were carried out using an AUTOLAB®, Eco Chemie, PGSTAT 30 electrochemical workstation in a potential range between −0.1 and 0.9 V versus Ag/AgCl at various scan rates of 5, 10, 20, 50,100, 125 and 150 mV s^{-1}. Further constant current charge–discharge tests were conducted in a potential range of −0.1 to 0.9 V versus Ag/AgCl, under various current densities of 0.1, 1, 3, 5 and 10 mA cm^{-2}.

3 Results and discussion

3.1 Characterization of the product

Based on the typical XRD pattern of the product shown in Fig. 1, one can easily conclude that all the peaks present can be very well indexed with a that of a body-centered tetragonal α-MnO_2 (space group I4/m), with lattice constants of $a = 0.9785$ nm, $c = 0.2863$ nm, in agreement with the standard values (JCPDS 44-0141). The diffraction peaks at 12.9°, 19.6°, 25.8°, 34.5°, 37.2°, 51.9°, 55.1°, 62.4°, 65.2° and 72.3° are the characteristic peaks of α-MnO_2, while no peaks which can be attributed to probable impurities was observed implying the high purity of the product. Consequently the product was concluded as being composed of pure α-MnO_2. The rather sharp reflection

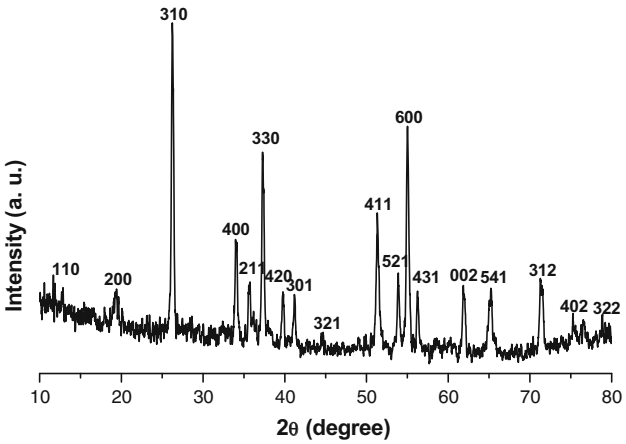

Fig. 1 XRD pattern of the prepared MnO_2 sample

peaks were also held as proof that the product enjoys high crystallinity. Additionally, FTIR studies were conducted on the sample and a typical FTIR spectrum of the product is given in Fig. 2. The peak at about 3416 cm^{-1} can be attributed to the vibrating mode the O–H band, resulting from the surface adsorption of traces of water. Further bands at 1639, 1435, 1116 and 1046 cm^{-1} were also attributed to the bending vibrations of –OH bound to the Mn atoms [21, 24]. In addition, the bands observed below 750 cm^{-1} were ascribed to the bending vibrations of Mn–O in the MnO_6 [37, 38] (Fig. 2).

Based on the morphological data on the MnO_2 sample, shown in Fig. 3, it can be concluded that sample was composed of nanoscale spheres with an average size of 100 nm, with secondary wall-like structures. It is actually evident that the particles have grown in wall-like patterns (Fig. 3b). The empry spaces among the building blocks of these wall-like structures faciliate the diffusion of the electrolyte into the structure of the material and are the foundations for the electrochemical properties of MnO_2. To

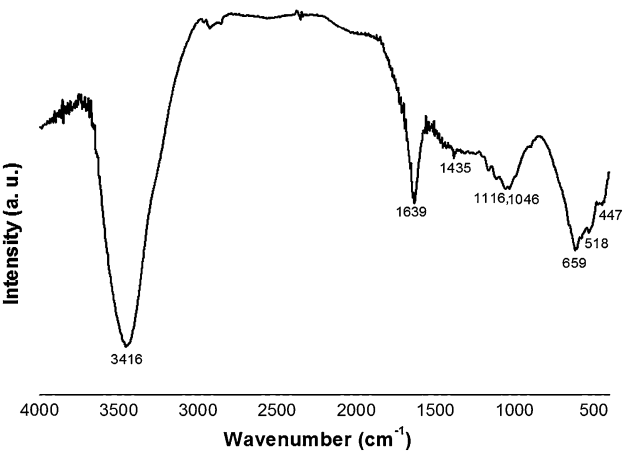

Fig. 2 IR spectrum of the prepared α-MnO_2 sample

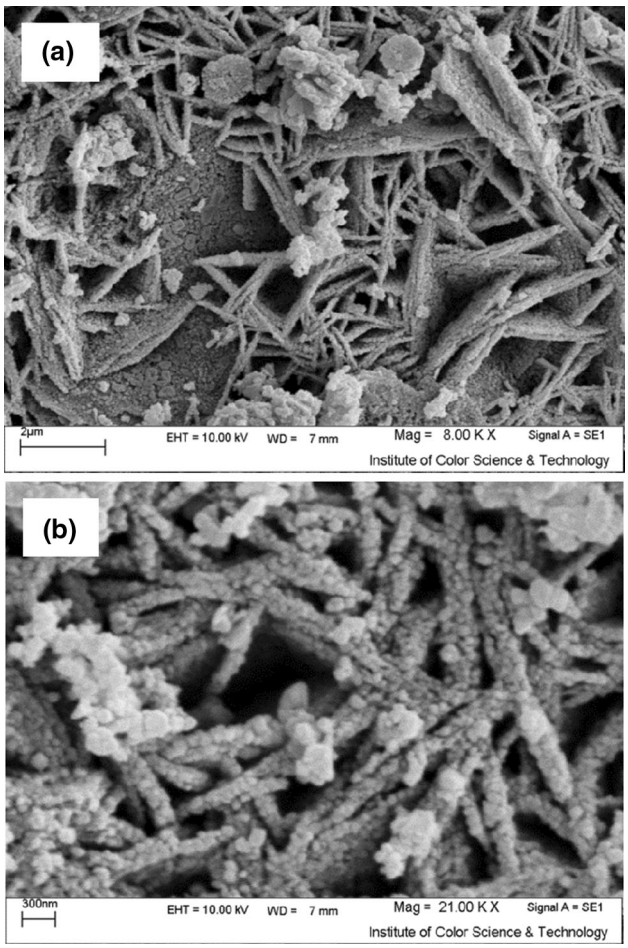

Fig. 3 SEM images of the prepared α-MnO_2 sample

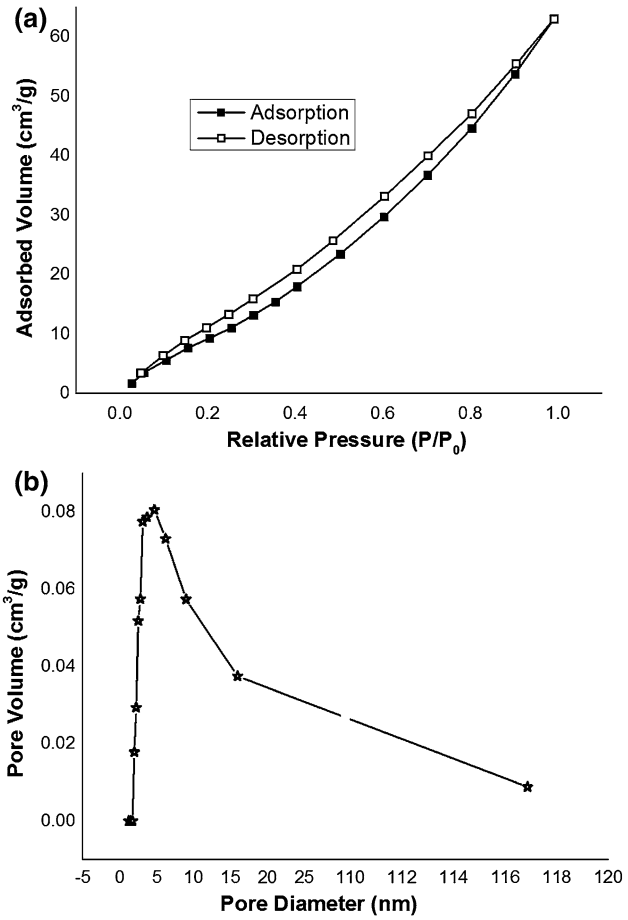

Fig. 4 **a** N_2 adsorption–desorption isotherms and **b** the BJH pore-size distribution curve of the prepared α-MnO_2 sample

evaluate the surface area of the MnO_2 particles Brunauer–Emmett–Teller (BET) method, where N_2 adsorption/desorption isotherm at 77 K is studied. Figure 4 reveals that the isoterm of the sample has a typical type III form with an H_2 type hysteretic loop. This can be held as proof of the presence of micro-porous sructure according to the IUPAC classification [39]. The hysterisis pattern furtehr proves the presence of complex and interconnected networks of pores of various different sizes and shapes [40] which is further supported by the SEM results (Fig. 3). Such a structure faciliates the diffusion of the electrolyte penetration and leads to proper electrochemical properties. Figure 4b illustrates the BJH pore-size distribution curve of the sample, which is indicative ofa relatively broad pore size distribution. On average the pore diameter and the surface area of the sample were calculated to be 3.8 nm and 57.4 $m^2\ g^{-1}$, respectively.

3.2 Evaluating the supercapacitive behavior

As shown in Fig. 5, the structure of α phase contains double chains of edge-sharing MnO_6 octahedrals. These

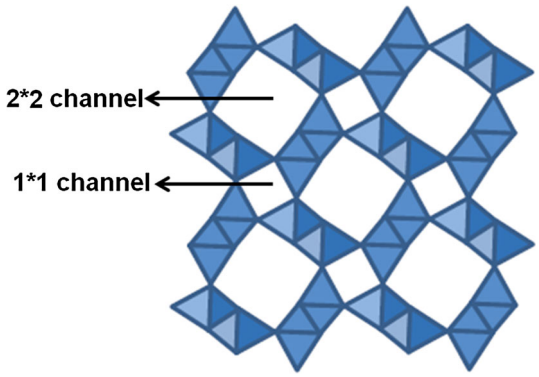

Fig. 5 Schematic view of α-MnO_2 crystal structure

octahedral are connected at the corners, forming one dimensional 2 × 2 and 1 × 1 pathways which extend parallel to the *c* axis of the tetragonal unit cell. The 2 × 2 tunnels are about 4.6 Å in diameter, can facilitate the intercalation/extraction of hydrated Na^+ cations, which are 3.58 Å in size [13]. Consequently, one can easily argue that the properties of the α-MnO_2 can host charge–discharge

through both mechanisms [41]. Figure 6a contains the cyclic voltammetric diagram acquired using working electrodes based on the produced MnO_2 in a 1 M aqueous Na_2SO_4 solution, at different scan rates ranging from 2 to 150 mV s^{-1}, in a potential range from −0.1 to 0.9 V versus Ag/AgCl. The voltammograms are rectangular (see inset in Fig. 6a.) and do not include any redox peaks. This shows that the electrode material has an ideal capacitive behavior.

Based on the increase in the size of the voltammograms increases upon increasing the sweep rate, the voltammetric currents are concluded to be directly proportional to the scan rate [42]. In the case of low-scan rates, the electrolyte ions find time to interact with sites available the electrode material, due to the period available to diffuse into all the sites. As a result higher capacitance values should be recorded in such cases. Oppositely, when the scan rate is high, the ions do not find the chance to access many sites in the active electrode material [41]. Interestingly, owing to the exceptional structure (i.e. large 2 × 2 pathways present in the structure of the electrode material), as well as the porosity (as seen in Fig. 3), and high surface area of the material confirmed by BET experiment (Fig. 4), no change was observed in the shape of the voltammograms upon increasing the scan rate in the experimental range which reached rates as high as 150 mV s^{-1}.

Through integrating the area of CV curves and given the equation below, the specific capacitances values were calculated and shown in Fig. 6b.

$$c = \frac{1}{mv(V_a - V_c)} \int_{V_a}^{V_c} I(V)\,\mathrm{d}V, \tag{4}$$

C is the specific capacitance (F g^{-1}), ΔV is the potential range (1 V), m is the mass of MnO_2 (g), v is the scan rate (V s^{-1}), and I(V) is the current response.

The results showed that the MnO_2-based working electrodes have the capability of delivering capacitances values

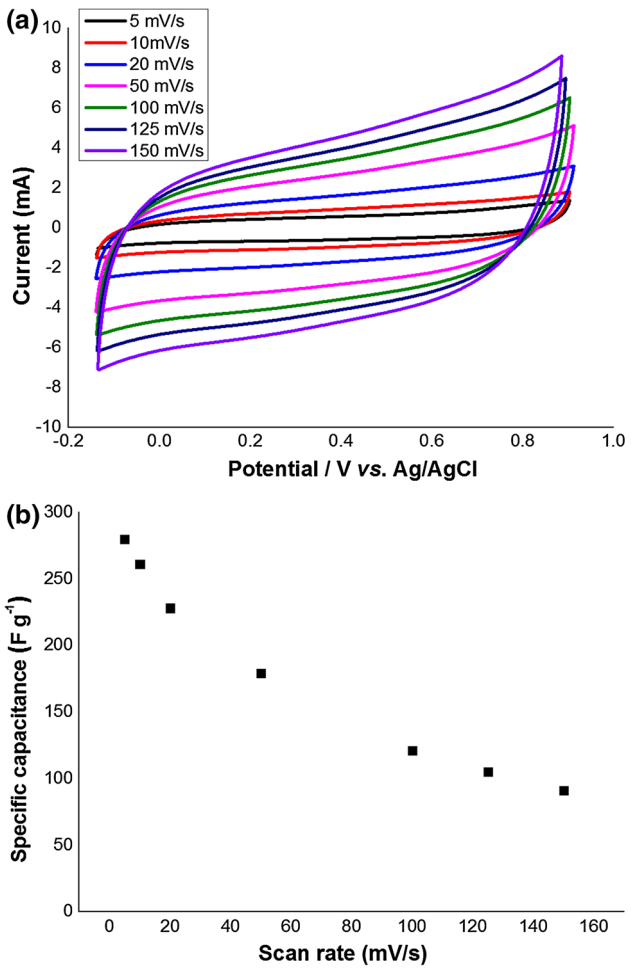

Fig. 6 **a** Cyclic voltammograms of the MnO_2 electrode and **b** the observed capacitances at different scan rates of 5–150 mV s^{-1}

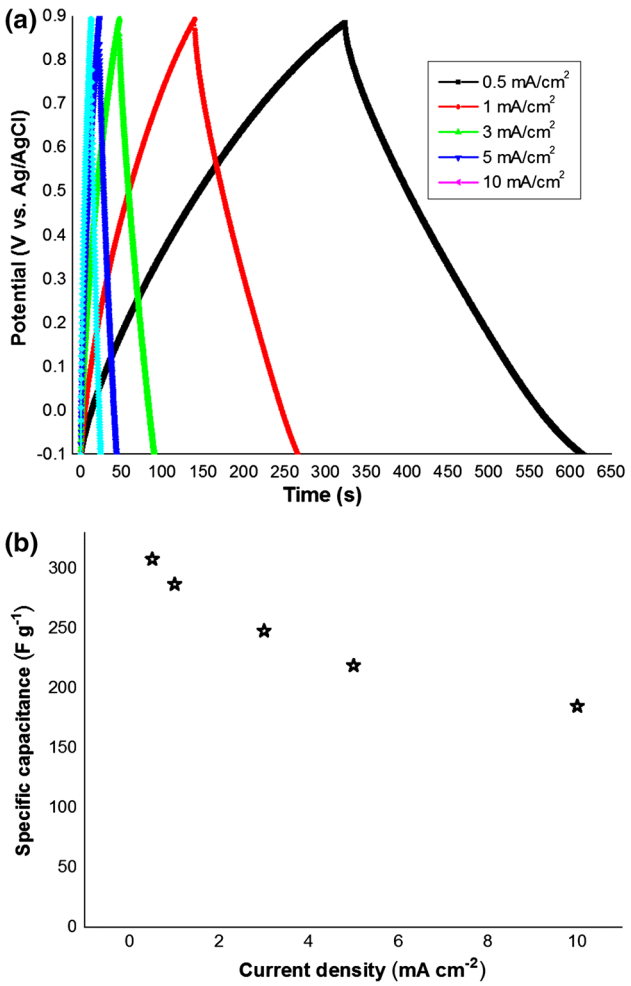

Fig. 7 **a** Charge–discharge profiles of the MnO_2 electrode in 1 M Na_2SO_4 at the different applied current densities of 0.5, 1, 3, 5 and 10 mA cm^{-2} and **b** the calculated specific capacitance at these applied currents

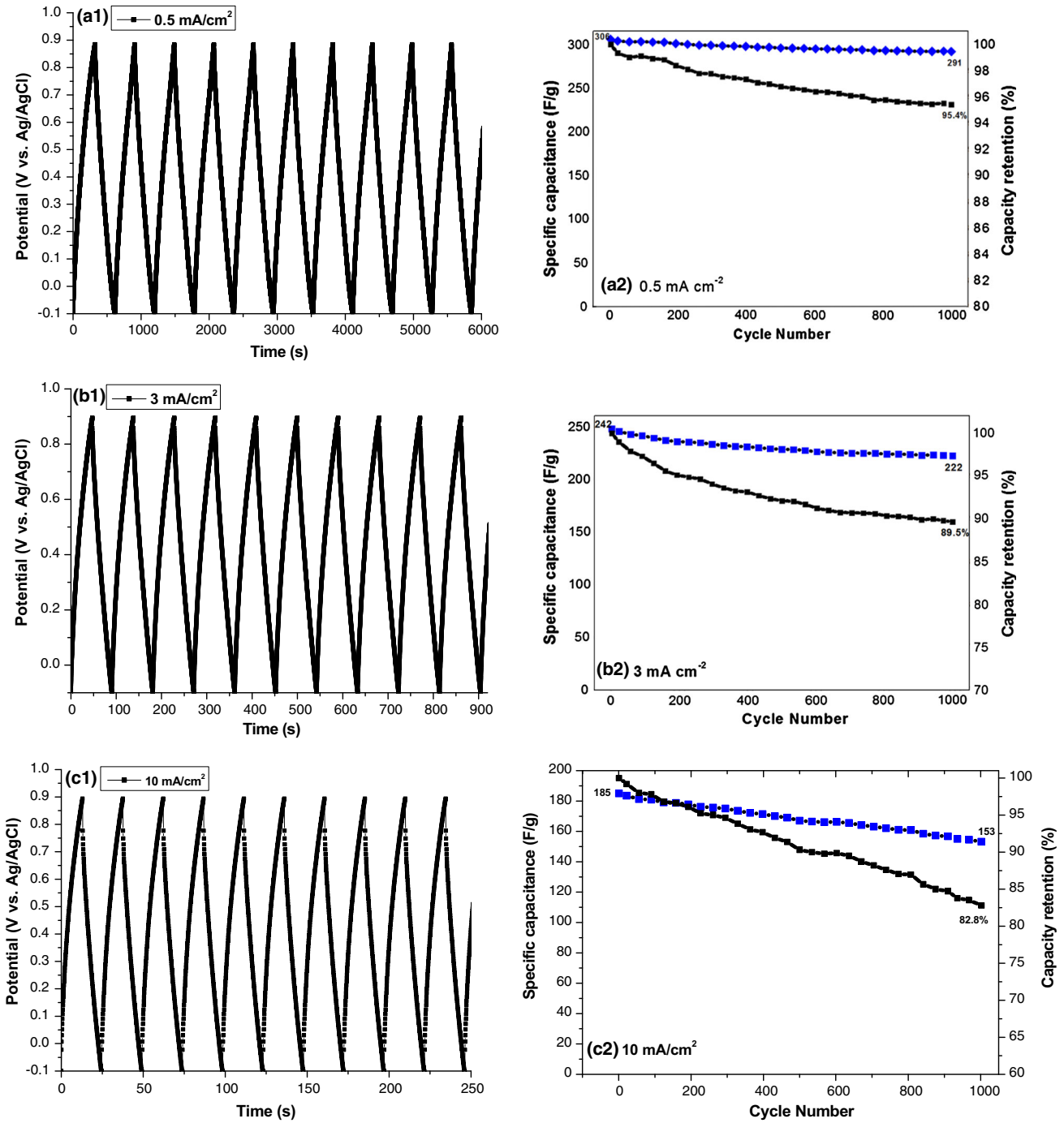

Fig. 8 **a** Charge–discharge curve (first ten cycles) of MnO_2 electrode at the current densities of 0.5, 3 and 10 mA cm^{-2}, **b** specific capacity and **c** capacity retention versus cycle number during 1000 cycles

of 280, 261, 228, 189,121, 105 and 91 F g^{-1} at the scan rates of 5, 10, 20, 50, 100, 125 and 150 mV s^{-1}, correspondingly. Figure 6b shows that increasing the scan rate directly affects the diffusion of Na^+ into the MnO_2 matrix and in turn the resulting capacitances values. When the scan rate is low (e.g. 5 mV s^{-1}), the Na^+ can easily diffuse into the material and reach almost all available sites in the electrode, leading to a complete insertion and hence an almost ideal capacitive behavior, which is reflected by the high capacitances values. At high scan rates (e.g. 150 mV s^{-1}), on the other hand, sodium ions do not have sample time to reach the same number of sites, only

reaching the superficial or surface sites of the electrode materials and hence the recorded capacitances values are rather low (Fig. 6b).

To have a deeper understanding of the supercapacitive behavior of the product galvanostatic charge–discharge tests were conducted using the MnO_2-based electrodes in the potential range of −0.1 to 0.9 V (vs. Ag/AgCl) and at current densities of 0.5, 1, 3, 5 and 10 mA cm^{-2} (Fig. 7a). The good linear potential-time behavior observed for all the curves, proved the MnO_2-based electrode to have a stable electrochemical performance in the 1 M Na_2SO_4 electrolyte, which is another characteristic behavior of an ideal capacitor.

The fact that no voltage drop was observed within the discharge process was attributed to the capacity of the electrode material. The observed charge–discharge patterns are in agreement with the result of the CV curves (Fig. 6a). The specific capacitance values can be calculated based on the data from the charge–discharge curves using the following relation:

$$C = [I \times \Delta t] / (m \times \Delta V)\ (F/g) \quad (5)$$

where I is the applied constant current (A), *m* is the mass of MnO_2, ΔV is the potential window during cycling and t_d is the discharge time of a cycle (s). Using this equation the capacitances values of the α-MnO_2 electrode were found to be 308, 278, 248, 189, 219 and 185 F g^{-1} at the applied current densities of 0.5, 1, 3, 5 and 10 mA cm^{-2}, respectively (Fig. 7b). These values are in agreement with the ones calculated based on the CV curves (Fig. 6b). In this light it can be further confirmed that the samples is capable of delivering a good supercapacitive behavior. In addition, the observed capacitances values are comparable with the values reported for nanostructured MnO_2 prepared in other works (i.e. 348 F g^{-1} at 0.2 mA cm^{-2} for samples prepared through a redox method [14], 218 F g^{-1} at 5 mV s^{-1} for α-MnO_2 nanorods/graphene composite prepared through a hydrothermal method [18], 338 F g^{-1} at 10 mV s^{-1} for the α-MnO_2 samples prepared by cathodic deposition [19], 291 F g^{-1} at 0.5 mA cm^{-2} for α-MnO_2 prepared through chemical bath deposition [23], 237 F g^{-1} at 2 mV s^{-1} for α, γ-MnO_2 nanowires prepared by galvanostatic electrodeposition [35], 237, 196 and 184 F g^{-1} at 2 A g^{-1} for amorphous MnO_2 films prepared by potentiodynamic, potentiostatic and galvanostatic electrodeposition modes [42]).

To evaluate the long-term electrochemical behavior of the MnO_2-based electrode, the galvanostatic charge/discharge cycling tests were performed. These tests were conducted at the different applied current densities between −0.1 and 0.9 V versus Ag/AgCl in 1 M Na_2SO_4 electrolyte. The characteristic charge–discharge profiles observed in the first ten cycles are given in Fig. 8a1–c1. The results revealed a good linear variation of potential during the charge–discharge processes, and illustrated the outstanding capacitance behavior of the prepared MnO_2 electrode under all the applied current densities (i.e. 0.5, 3 and 10 mA cm^{-2}). The charge–discharge times acquired for the MnO_2-based electrodes were almost identical, indicating the high reversibility and coulombic efficiency of the electrode material. The specific capacitance of each cycle, under the applied current density, was calculated using Eq. (4) and the results are given in Fig. 8a2–c2. Based on these values, the capacity retention of the MnO_2 electrode on cycling was evaluated. The calculations indicate that the prepared α-MnO_2 are capable to exhibit excellent capacity retentions of 95.4, 89.5 and 82.8 % after 1000 charge–discharge cycles at the current densities of 0.5, 3 and 10 mA cm^{-2}, respectively. The results further indicated the excellent electrochemical performance of the product.

4 Conclusion

A simple cathodic deposition procedure was applied to produce nanostructured α-MnO_2 through deposition from a nitrate bath, under a current density of 0.1 mA cm^{-2}. The electrochemical evaluations of the sample through cyclic voltammetry and charge–discharge techniques indicated its excellent electrochemical behaviors like specific capacitances of 280, 261, 228, 189, 121, 105 and 91 F g^{-1} at scan rates of 5, 10, 20, 50, 100, 125 and 150 mV s^{-1}, respectively. Further, excellent long-term cycling stabilities of 95.4, 89.5 and 82.8 % were observed after 1000 charge–discharge cycles. These results proved the prepared MnO_2 nanostructures to have the potentials for use as an excellent electrode material of supercapacitors.

References

1. M. Huang, F. Li, F. Dong, Y.X. Zhang, L.L. Zhang, J. Mater. Chem. A (2015). doi:10.1039/C5TA05523G
2. P. Wang, Y.J. Zhao, L.X. Wen, J.F. Chen, Z.G. Lei, Ind. Eng. Chem. Res. **53**, 20116 (2014)
3. J. Yan, Z. Fan, T. Wei, M. Zhang, J. Mater. Sci.: Mater. Electron. **21**, 619 (2010)
4. Z. Li, Z. Liu, D. Li, B. Li, Q. Li, Y. Huang, H. Wang, J. Mater. Sci.: Mater. Electron. **26**, 353 (2015)
5. Z. Su, C. Yang, B. Xie, Z. Lin, Z. Zhang, J. Liu, B. Li, F. Kang, C.P. Wong, Energy Environ. Sci. **7**, 2652 (2014)
6. G. Wang, L. Zhang, J. Zhang, Chem. Soc. Rev. **41**, 797 (2012)
7. M. Aghazadeh, M. Ghannadi Maragheh, M.R. Ganjali, P. Norouzi, F. Faridbod, Appl. Surf. Sci. **364**, 141 (2016)
8. X. Su, X. Yang, L. Yu, G. Cheng, H. Zhang, T. Lin, F.H. Zhao, Cryst. Eng. Comm. **17**, 5970 (2015)
9. M.J. Young, A.M. Holder, S.M. George, C.B. Musgrave, Chem. Mater. **27**, 1172 (2015)

10. S. Devaraj, N. Munichandraiah, J. Phys. Chem. C **112**, 4406 (2008)
11. S.L. Brock, N. Duan, Z.R. Tian, O. Giraldo, H. Zhou, S.L. Suibm, Chem. Mater. **10**, 2619 (1998)
12. R. Ma, Y. Bando, L. Zhang, T. Sasaki, Adv. Mater. **16**, 918 (2004)
13. Y. Zhang, C. Sun, P. Lu, K. Li, S. Song, D. Xue, Cryst. Eng. Commun. **14**, 5892 (2012)
14. M. Musil, B. Choi, A. Tsutsumi, J. Electrochem. Soc. **162**, A2058 (2015)
15. Y. Chen, J. Xu, Y. Yang, Y. Zhao, W. Yang, X. He, S. Li, C. Jia, J. Mater. Sci.: Mater. Electron. **8**, 1 (2015)
16. W. Chen, X. Tao, D. Wei, H. Wang, Q. Yu, Y. Li, J. Mater. Sci.: Mater. Electron. (2015). doi:10.1007/s10854-015-3897-z
17. M. Kim, Y. Hwang, J. Kim, J. Mater. Sci. **48**, 7652 (2013)
18. S.X. Deng, D. Sun, C. Wu, H. Wang, J.B. Liu, Y.X. Sun, H. Yan, Electrochim. Acta **111**, 707 (2013)
19. T. Yousefi, A. Nozad Golikand, M.H. Mashhadizadeh, J. Solid State Chem. **190**, 202 (2012)
20. U.M. Patil, J.S. Sohn, S.B. Kulkarni, H.G. Park, Y. Jung, K.V. Gurav, J.H. Kim, S.C. Jun, Mater. Lett. **119**, 135 (2014)
21. X. Su, L. Yu, G. Cheng, H. Zhang, M. Sun, X. Zhang, Appl. Energy **153**, 94 (2015)
22. X.J. Li, Y. Zhao, W.G. Chu, Y. Wang, Z.J. Li, P. Jiang, X.C. Zhao, M. Liang, Y. Liu, RSC Adv. **5**, 77437 (2015)
23. N.R. Chodankar, D.P. Dubal, G.S. Gund, C.D. Lokhande, Electrochim. Acta **165**, 338 (2015)
24. X. Zhang, X. Liu, B. Li, Q. Chu, Y. Wang, X. Zhao, X. Wang, J. Mater. Sci.: Mater. Electron. **24**, 2189 (2013)
25. G.H. Annal Therese, P. Vishnu Kamath, Chem. Mater. **12**, 1195 (2000)
26. I. Zhitomirsky, Adv. Colloid Interface Sci. **97**, 277 (2002)
27. E.H. Liu, R. Ding, X.Y. Meng, S.T. Tan, J.C. Zhou, J. Mater. Sci.: Mater. Electron. **18**, 1179 (2007)
28. F. Xiao, Y. Xu, J. Mater. Sci.: Mater. Electron. **24**, 1913 (2013)
29. G. Wang, W. Wang, Y. Zhao, G. Shao, T. Liu, Z. Ma, Ionics **20**, 243 (2014)
30. S. Liu, Y. Liu, W. Song, J. Song, C. Wang, G. Shao, X. Qin, J. Solid State Electrochem. **19**, 1321 (2015)
31. S.A. Hashmi, H.M. Updahyaya, Ionics **8**, 272 (2002)
32. E. Preisler, J. Appl. Electrochem. **19**, 559 (1989)
33. H. Xia, M.O. Lai, L. Lu, JOM **63**, 54 (2011)
34. Y. Su, I. Zhitomirsky, Adv. Eng. Mater. **16**, 760 (2014)
35. T. Yousefi, A. Nozad Golikand, M.H. Mashhadizadeh, M. Aghazadeh, Curr. Appl. Phys. **12**, 193 (2012)
36. M. Aghazadeh, M. Asadi, M. Ghannadi Maragheh, M.R. Ganjali, P. Norouzi, F. Faridbod, Appl. Surf. Sci. **364**, 726 (2016)
37. J. Tizfahm, M. Aghazadeh, M. Ghannadi Maragheh, M.R. Ganjali, P. Norouzi, F. Faridbod, Mater. Lett. **167**, 153 (2016)
38. H.E. Wang, D. Qian, Mater. Chem. Phys. **109**, 399 (2008)
39. F. Rouquerol, J. Rouquerol, K. Sing, *Adsorption by powders and porous solids: principles, methodology and applications* (Academic Press, Cambridge, 1999)
40. G.J. Soler-Illia, C. Sanchez, B. Lebeau, J. Patarin, Chem. Rev. **102**, 4093 (2002)
41. W. Wei, X. Cui, W. Chena, D.G. Ivey, Chem. Soc. Rev. **40**, 1697 (2011)
42. D.P. Dubal, D.S. Dhawale, T.P. Gujar, C.D. Lokhande, Appl. Surf. Sci. **257**, 3378 (2011)